PCCP
Physical Chemistry Chemical Physics

Accepted Manuscript

This article can be cited before page numbers have been issued, to do this please use: T. Wei, V. Balevicius, T. Polivka, A. Ruban and C. D.P. Duffy, *Phys. Chem. Chem. Phys.*, 2019, DOI: 10.1039/C9CP03574E.

View Article Online
DOI: 10.1039/C9CP03574E

PCCP

ARTICLE TYPE

Cite this: DOI: 10.1039/xxxxxxxxxx

How carotenoid distortions may determine optical properties: Lessons from the Orange Carotenoid Protein†

Tiejun Wei[a], Vytautas Balevičius Jr.[a], Tomás Polívka[b], Alexander V. Ruban[a] and Christopher D. P. Duffy[a,*]

Received Date
Accepted Date

DOI: 10.1039/xxxxxxxxxx

www.rsc.org/journalname

Carotenoids in photosynthetic proteins carry out the dual function of harvesting light and defending against photo-damage by quenching excess energy. The latter involves the low-lying, dark, excited state labelled S_1. Here "dark" means optically-forbidden, a property that is often attributed to molecular symmetry, which leads to speculation that its optical properties may be strongly-perturbed by structural distortions. This has been both explicitly and implicitly proposed as an important feature of photo-protective energy quenching. Here we present a theoretical analysis of the relationship between structural distortions and S_1 optical properties. We outline how S_1 is dark not because of overall geometric symmetry but because of a topological symmetry related to bond length alternation in the conjugated backbone. Taking the carotenoid echinenone as an example and using a combination of molecular dynamics, quantum chemistry, and the theory of spectral lineshapes, we show that distortions that break this symmetry are extremely *stiff*. They are therefore absent in solution and only marginally present in even a very highly-distorted protein binding pocket such as in the Orange Carotenoid Protein (OCP). S_1 remains resolutely optically-forbidden despite any breaking of bulk molecular symmetry by the protein environment. However, rotations of partially conjugated end-rings can result in fine tuning of the S_1 transition density which may exert some influence on interactions with neighbouring chromophores.

1 Introduction

Carotenoids (Cars) have been intensively studied for decades due (among other things) to their essential roles in photosynthetic light-harvesting[1,2]. Among many other functional roles they are essential to Non-Photochemical Quenching (NPQ), a mechanism by which plants avoid photo-damage through the dissipation ('quenching') of excess energy in the Photosystem II (PSII) antenna complex.[2–4].

The light-harvesting and NPQ roles of large Cars are (broadly) defined by two excited electronic states. The second singlet excited state, S_2, is the first optically (one-photon) accessible excitation. It gives rise to strong absorption blue-green and shows a classic three-peak vibronic progression characteristic of the optically-active C=C and C-C symmetric stretching modes[5–7]. The position of the S_2 0-0 line depends strongly on the conjugation length of the Car, both in absolute terms between different Cars and in terms of structural distortions such as isomerization and end-group rotation that affect the *effective* conjugation length[8,9]. S_2 is responsible for efficient Car light-harvesting in photosynthetic antenna complexes, with energy transfer to the (B)Chl Qx state occurring on an ultra-fast (<100 fs) timescale[10].

S_1, is optically (one-photon) forbidden. Two-photon absorption spectra of β-carotene and lutein show that it is of similar width to the S_2 transition with a hint of a similar vibronic structure[11]. For the Cars found in plant antenna complexes the S_1 0-0 transition lies in the 14000-15000 cm^{-1} region[7]. It also has a very short excited lifetime (2-20 ps[7]) which is why Cars such as lutein[12] and zeaxanthin[4] function as (or part of) the molecular species responsible for excess energy dissipation during NPQ. Although the exact details of the process are still debated (for comprehensive discussions see[2–4,13]) it essentially involves the opening-up (in high light) of an energy transfer pathway from the Chl a Q_y state to S_1. The key parameter is the resonance coupling between them[14] which is defined by the magnitudes and relative orien-

[a] School of Biological and Chemical Sciences, Queen Mary University of London, London E1 4NS.
[b] Institute of Physics and Biophysics, University of South Bohemia in Czech Republic, Czech Republic
* Corresponding author: c.duffy@qmul.ac.uk

† Electronic Supplementary Information (ESI) available: (1) Force field parameters for Echinenone (2) Validation of the Echinenone FF. (3) Supplementary data for the 2D end-ring dihedral surfaces. (4) Additional details concerning the calculation of S_1 absorption lineshapes. (5) Visual illustrations of the normal mode decomposition of arbitrary Echinenone distortions. See DOI: ...

View Article Online
DOI: 10.1039/C9CP03574E

tation of their transition dipole moments (TDMs), although the dependence can be non-trivial given to small inter-pigment distances. Theoretical models of the major PSII antenna protein, LHCII, propose quenching arises from weak couplings that are turned on and off by small changes in relative orientation[15]. The weak nature of these interactions arises from the fact that S_1 has a very small TDM[16]. However, it is also possible that the NPQ switch involves an increase in to the S_1 dipole length itself. Recently, Son *et al.* measured ultra-fast (<400 fs) energy transfer from Chl a to lutein in quenched LHCII, possibly indicating very strong couplings[17].

It is often proposed that S_1 may acquire an increased dipole length if the Car is distorted away from the equilibrium, *all-trans* geometry. The weak fluorescence from S_1 has been attributed to cis-isomerization making the state optically-allowed[18], although this is undermined by the fact that S_1 absorption is almost entirely absent, even for Cars such as the 9-cis neoxanthin[19]. Red absorption features in crystals of Car-binding proteins such as the Orange Carotenoid Protein (OCP)[20] and the Helical Carotenoid Proteins (HCPs) have been discussed in terms of an optically-allowed S_1 state created by a very distorted structure, although in the latter case this was dismissed in favour of some (unknown) effect of long-range order in the crystal. Lastly, Ligouri *et al.* reported femto-second spectroscopic measurements on a perpetually-quenched mutant of LHCII that binds only one type of Car: astaxanthinz[21]. They identified several S_1-like signals which differ in energy, lifetime and coupling to Chl *a* which they attributed to different distorted forms of the pigment. One of these "states", S_q, was found to be a responsible for the majority of the quenching.

It is commonly stated, particularly in the photosynthetic literature, that S_1 is "symmetry forbidden" with the implied symmetry being *coordinate inversion*. The ground state (S_0), S_1 and S_2 are often given the labels 1^1Ag, 2^1Ag and 1^1Bu respectively. *Ag* or *Bu* denote states that are even or odd under inversion and optical selection rules imply that one-photon transitions between states of the same symmetry are forbidden. Geometry distortions break this symmetry and in principle this restriction will no longer apply. This is the exact mechanism behind the appearance of the blue "cis-band" in Car absorption which is due to a high-lying *Ag* state[22]. However, cis-isomerization does not generally induce detectable S_1 absorption meaning additional factors must dictate it's properties. Recently, Fiedor *et al.* argued that even *all-trans* Cars do not possess well-defined inversion symmetry and therefore the derived selection rules do not apply[23]. Instead they propose that S_1 is optically inaccessible due to a large displacement from the equilibrium ground state. However, if so the behaviour of the cis-band is difficult to explain. Moreover, S_1 is clearly accessible from S_0 by either two-photon absorption[11] or energy transfer from another pigment[24].

The optical properties of S_1 are in fact related to *alternancy*, or particle-hole (p-h), symmetry[25,26]. Often S_0, S_1 and S_2 are given the extended labels 1^1Ag^-, 2^1Ag^- and 1^1Bu^+ respectively with $+/-$ indicating even/odd p-h symmetry. It is a topological symmetry related to the degree of π-conjugation along the carbon backbone and is therefore little-effected by loss of inversion symmetry through isomerization. It was later shown that $'-'$ states are strongly-correlated, meaning that they have a strong multi-electron character[27,28]. This is a critical point since pure multi-electron transitions are completely optically forbidden (they have no one-electron transition density)[29]. Although p-h symmetry is not exact, even for linear polyenes, it is convenient short-hand for the relationship between π-conjugation, electron correlation and optical properties. S_1 has a very small dipole moment because is has a very small transition density due to π-conjugation and not inversion symmetry. Incidentally, the cis-band is sensitive to loss inversion symmetry because it originates from weakly-correlated Ag^+ states. The reader is directed to a thorough review article[30] and classic book on these topics[31]. Things are more complex when we consider non-equilibrium distortions. A simple quantification of the degree of conjugation is the bond length alternation (BLA), the average difference between neighbouring C=C and C-C bond lengths normalized by the total length of the chain[32]. Loco *et al.* showed that that for the Car astaxanthin in the protein crustcyanin the binding pocket induced fluctuations in BLA which effected the energy of the S_2 state[33]. Calculations have shown that *ad hoc* alterations in BLA in planar Cars (by using different quantum chemical optimization methods) can in principle alter the S_1 TDM[34,35]. Combining these two observations we hypothesize that a protein binding pocket may be capable of tuning S_1 optical properties through perturbations to conjugation.

Here we investigate the relationship between geometry distortions and S_1 and S_2. We use the example of Echinenone (Ech) *in vacuuo*, in THF and bound by the orange (dark-adapted) form of OCP, OCP_o. We do not address the actual biological function of OCP and for an in depth discussion the reader is directed to refs.[36,37]. OCP_o is an ideal system for our purposes as it is water soluble (making our simulations simpler) and contains only one chromophore (Ech) which is severely distorted by the binding pocket[38]. Moreover, Ech in OCP_o has a significantly red-shifted absorption relative to the solvent and crystals of OCP_o display a weak red absorption feature that has been tentatively associated with an "allowed S_1"[20]. We address two types of non-equilibrium distortions: end-ring rotations and general non-planar distortions to the back bone. The latter are analyzed within the context of *normal distortions* and BLA. For completeness we also consider backbone isomerization (equilibrium distortions). We first consider ad hoc distortions to Ech *in vacuo* before considering dynamic fluctuations within the solvent distortions enforced by the OCP_o binding pocket.

2 Methods and Computational Details

2.1 Quantum Chemical Calculations

Calculation of Ech geometries, vibrational normal modes, and excited electronic states were required for parameterizing/validating our Force Field (FF) for Ech, generating *ad-hoc* distorted structures, and providing a basis set for describing arbitrary non-planar distortions. The initial structure of Ech was taken from the OCP_o crystal structure 5TUX[20]. Optimized reference geometries were calculated using the B3LYP hybrid exchange-correlation functional[39] and the 6-311G(d,p) basis set[40,41] (as

View Article Online
DOI: 10.1039/C9CP03574E

implemented in Gaussian 09[42]) as this has been shown to accurately reproduce the BLA distribution along the conjugated chain[35]. For Ech the conjugation extends into both end-rings and the global minimum corresponds to both in the *cis* configuration (hereafter *cis-cis*). In OCP$_o$ Ech exists in a highly-distorted *cis-trans* configuration (with the *trans* referring to the keto end-ring, ε_1) and so a *cis-trans* reference geometry was obtained by relaxing Ech from OCP$_o$ into the closest local minimum (see Fig. 1 a). To explore specific distortions a sequence of optimized backbone *cis*-isomers were produced using the same method, namely *R*1 to *R*5 (see Fig. 1 A). To explore the effects of end-ring rotations a 2D scans of ε_1 and ε_2 (see Fig. 1 A) were produced in increments of 15 deg followed by a standard re-optimization process in which ε_1 and ε_2 are constrained. normal mode analyses were performed *in vacuuo* for the *cis-cis* and *cis-trans* reference structures using the same DFT method B3LYP/6-311G(d,p).

We calculated the Ech excited states using the AM1/MNDO-MECI with an active space of 8 π-orbitals ($HOMO-3,...,HOMO,LUMO,...,LUMO+3$) as implemented by the MOPAC semi-empirical quantum chemistry package[43]. The orbital active space for the equilibrium geometry and various distorted structures are visualized in the ESI (Supp. Figs. 1-5). The validity of this method for calculating Car excited states was initially demonstrated by Kusumoto *et al.*[44] and has previously been used to study *ad hoc* geometry distortions to the Car lutein[45]. We have used it extensively to parameterize models of excitation quenching in plant LHCs[14,46–48]. As we show later it accurately reproduces the absorption spectrum of Ech. and qualitatively reproduces the vibronic structure of S_1.

2.2 Echinenone Force Field Parameterization

Prandi *et al.* recently published a protocol for developing finely-parameterized AMBER[49] FFs for Cars[35]. These FFs allow for direct calculation of excited electronic states from Molecular Dynamics (MD) snapshots. Here we used their zeaxanthin (Zea) parameters as a basis for Ech (it differs from Zea only in the absence of hydroxyl groups in both end-rings and the presence of a keto group in one). For parameters that could not be directly taken from Zea we used the Paratool plugin for the Visual Molecular Dynamics (VMD) package[50]. All atomic charges for Ech were calculated using the Restrained Electrostatic Potential (RESP) method[51] with a B3LYP/6-311G(p,d) ESP for *cis-cis* Ech. Bond and angle parameters were largely assigned by chemical analogy to Zea however those associated with the points of difference - the additional keto group and the missing hydroxyl groups - were calculated. This accounts for a total of 6 bonds and 6 angles. A B3LYP/6-311G(d,p) normal mode calculation for *cis-cis* Ech *in vacuo* provides a reference. Paratool then generates bond and angle parameters to reproduce this quantum chemical target data. We discard those parameters already obtained from Zea and retain the missing ones. Prandi *et al.* found that further refinement of parameters calculated in this manner are required. This takes the form of slight re-scaling. A list of these factors by bond/angle type are given in the ESI of ref.[35]. We re-scaled these new parameters accordingly, although since they are not part of the conjugation path they are not critical to subsequent calculations. Dihedral parameters were also obtained, where possible, by analogy to Zea. The missing dihedrals (again in the end-rings) were taken from the Generalized AMBER Force Field (GAFF). Exceptions were made for end-ring rotations for which the GAFF under-estimates barriers. These were re-assigned in accordance with those calculated in our 2D dihedral scan. Lastly, all Lennard-Jones parameters were assigned according to the GAFF (as they had been for Zea). For verification we considered its ability to reproduce the BLA and normal mode distribution of the quantum chemical structures. We also verified that the average S_1 and S_2 excitation energies and TDMs calculated for *in vacuuo* MD runs matched those calculated the single point calculation for the quantum chemical structures. The FF parameters, along with a detailed discussion of the validation of the FF is given in the ESI.

2.3 Molecular Dynamics Simulations of Echinenone and OCP$_o$

We produced MD simulations of *cis-cis* Ech in THF (tetrahydrofuran) and Ech bound to OCP$_o$ in water. The starting structure for OCP$_o$ was the 1.5 Å X-ray structure (PDB: 5TUX) reported by Bandara et al.[20]. The Ech-THF simulations were carried out in periodic box set so that Ech was at least 20 Å from the box edge and the GAFF was used for the explicit THF solvent. For OCP$_o$ the ff14SB AMBER FF was used for the apoprotein and the GAFF was used for the glycerol ligand. A small disordered loop region was re-constructed using the MODELLER package[52]. OCP$_o$ was solvated in a 20 Å box of explicit TIP3P water. In each case, following a brief initial minimization, the system was equilibrated for 20 ps, with the temperature rising from 0 - 300 K. This was followed by a 20 ps NPT run with a constant temperature of 300 K enforced by a Langevin thermostat with a characteristic relaxation time of 1 ps. For Ech-THF 5 repeat production runs of 1 ns each were performed (with a 0.5 fs time step), which is sufficient to give a statistical picture of fluctuations around the equilibrium structure. For OCP$_o$ 5 repeat production runs of 50 ns were performed (0.5 fs time step), with the longer time needed for the more complex dynamics. Although 50 ns is not sufficient to probe protein conformational changes (this is not the purpose of the study) it is perfectly adequate to study fluctuations about the relaxed crystal structure. All MD simulations were performed using the AMBER 16[49] and NAMD[53] packages.

For statistical characterization of Ech distortions and excited state properties 1000 snapshots were taken from each trajectory, giving a sample of 5000 each for Ech-THF and OCP$_o$. For prediction of absorption spectra we took several 40 ps fragments from each trajectory and sampled a total of 20000 snapshots (giving a time resolution of 2 fs).

2.4 Normal Mode Decomposition of Distorted Structures

The range of general, non-planar distorted geometries that Ech can adopt represents a very large phase space. However, an arbitrary static distortion can be represented as a linear superposition of distortions along a finite number of normal modes, so-called *normal distortions*[54,55]. Within the harmonic approximation the

View Article Online
DOI: 10.1039/C9CP03574E

following definition is exact,

$$\mathbf{D'}_{dist} = \mathbf{T}_{xyz}(v_x, v_y, v_z)\mathbf{R}_{xyz}(\alpha, \beta, \gamma)\left(\mathbf{D}_{ref} + \sum_{i}^{3N-6} a_i \Delta_i\right) \quad (1)$$

where $N = 95$ is the number of atoms in Ech, $\mathbf{D'}_{dist}$ is a $3 \times N$ matrix whose columns are Cartesian atomic coordinates of a distorted Ech snapshot, and $\mathbf{D}_{ref}$ is a quantum chemically optimized reference structure (either *cis-cis* or *cis-trans*). Δ_i is a $3 \times N$ matrix of normalized Cartesian atomic displacements for the i^{th} normal mode, and a_i are the expansion coefficients. The Cartesian displacements are taken from the DFT frequency analysis on our reference structures and the sum is over the complete set of all $3N-6$ normal modes. Assuming a general reference structure we will also need to perform 3 rigid-body rotations, defined by the 3D rotation matrix $\mathbf{R}_{xyz}(\alpha, \beta, \gamma)$ and a translation into the centre-of-mass frame of the snapshot, $\mathbf{T}_{xyz}(v_x, v_y, v_z)$. In principle we can then obtain the normal distortion amplitudes, a_i, rotation angles, (α, β, γ) and translations, (v_x, v_y, v_z) as fitting parameters. However, the exact solution of such a high dimensional optimization problem is possible but at great computational cost. To simplify the Ech snapshots were first superimposed onto the reference structure to allow us to neglect translation and rotation induced during the MD run. This is done by minimising the Root-Mean-Square atomic coordinate Deviation (RMSD) of the backbone carbons. The approximate representation of the distortion is then,

$$\mathbf{D}_{dist}^{rot-trans} \approx \mathbf{D}_{ref} + \sum_{i}^{3N-6} a_i \Delta_i \quad (2)$$

Where $\mathbf{D}_{dist}^{rot-trans}$ represent the Cartesian coordinate of the re-aligned Ech snapshot. An example of such an approximate fit can be found in the ESI (Supp. Fig. 10). Lastly, it is important to remember that the normal distortions are merely a convenient basis for describing general shapes and that actual significant distortions of the molecule along a single high frequency mode are not energetically accessible at room temperature.

2.5 Absorption spectrum reconstruction from MD

We calculated the absorption spectra of Ech based purely from the S_2 and S_1 transition energies and oscillator strengths calculated for a series of closely-spaced MD snapshots. From this we obtained the spectral density[56,57], which in turn enters the expression for linear absorption via the *line-shape function*[58]. To determine the spectral density, we employed a procedure in line with the work of Valleau et al.[59] using 40 ps trajectory fragments with a time resolution of 2 fs. We denote the excitation energy at time step t_i as E_i, where the index i runs through the N time points. The time-discrete auto-correlation function of the S_2 (or S_1) excitation energy is then calculated as[59–61],

$$C(t_k) = \frac{1}{N-k}\sum_{i=1}^{N-k}(E_i - \bar{E})(E_{i+k} - \bar{E}) \quad (3)$$

where $\bar{E}$ is the mean energy of the sampled data. To minimize the spurious effects (e.g. negative values and noise) in the Fourier transform, a Gaussian filter of unit area in the frequency domain is applied[59]. As the calculated correlator is a classical function, its Fourier transform does not immediately yield the spectral density (which also accounts for quantum effects[58]. Hence we additionally apply a semi-classical correction term $\frac{1}{\pi}\tanh(\frac{\omega\beta}{2})$ (β is the inverse temperature; we set $\hbar = 1$)[59], by which we multiply the auto-correlation function in the frequency domain. The end result is the spectral density that can be used to calculate the line-shape function and in turn the absorption spectrum.

For computational simplicity we fit an analytical ansatz spectral density to the discrete numerical one. This is similar to the strategy by Olbrich et al.[60] except that they applied an analytical ansatz to the correlation function itself, whereas we obtain an analytical expression for the spectral density as the last step. Our ansatz contained three under-damped terms[57] and one over-damped term for the lowest frequencies[58]. Such a decomposition is in line with the earlier observation that the Car spectral density can be accurately described by a simple model with a small number of under-damped terms representing the high-frequency C-C/C=C stretching modes[14,48]. The absorption spectrum is then obtained via Fourier transform of linear response function.

3 Results

3.1 Excited states of Echinenone

The calculated equilibrium geometries for *cis-cis* and *cis-trans* Ech, along with the back-bone isomers $R1 - R5$ (see Fig. 1 **A**) are consistent with previous DFT studies, as are the vibrational normal modes[62]. AM1-MECI-OPEN(8,8) gives a chemically realistic description of S_1 and S_2. S_2 is an ionic excitation with approximate *Bu* symmetry and a predominantly single $HOMO \rightarrow LUMO$ character, approximately consistent with the $^1Bu^+$ label. Its excitation energy is $E_{S_2} = 2.71$ eV which is in qualitative agreement with the experimental value of 2.50 eV[62]. The magnitude of the TDM is $|\mu_{S_2}| = 53.2$ D which represents an over estimate of $2-3$ when compared to ab initio calculated values of $15-20$D[63]. Generally the Car S_2 TDM falls within this range and we scaled all subsequent TDM by a factor of 3. The calculated S_1 state is a covalent excitation with approximate *Ag* symmetry. It's electronic character is largely double $HOMO \rightarrow LUMO$ ($C_{H,H}^{L,L} \approx 0.56$), which implies $^1Ag^-$, but with some contribution from the $^1Ag^+$-type $HOMO \rightarrow LUMO+1$ ($C_H^{L+1} \approx 0.23$) and $HOMO-1 \rightarrow LUMO$ ($C_{H-1}^{L} \approx 0.24$) single electron transitions. The calculated excitation energy ($E_{S_1} = 2.51$ eV) is overestimated with respect to the 1.77 eV observed via excited state absorption[64]. However, this technique probes the relaxed S_1 state and the vertical energy will be significantly larger. The calculated S_1 TDM is significantly smaller than for S_2 but noticeably non-zero, $|\mu_{S_1}| = 6.48$ D. We attribute this to two factors. Firstly, as in peridinin[34] we do expect a small but non-zero TDM ($|\mu_{S_1}| > 1.0$ D) arising from the keto-group. Secondly, whatever TDM S_1 possesses is due to mixing with S_2 and we notice a 1% contribution from single $HOMO \rightarrow LUMO$ ($C_H^L \approx 0.10$). Since the TDM of S_2 is systematically over-estimated by a factor of 3, we assume the same is true for S_1 and apply the same correction to all subsequent calculations. In our previous studies[14,46,47] we have noticed that the

View Article Online
DOI: 10.1039/C9CP03574E

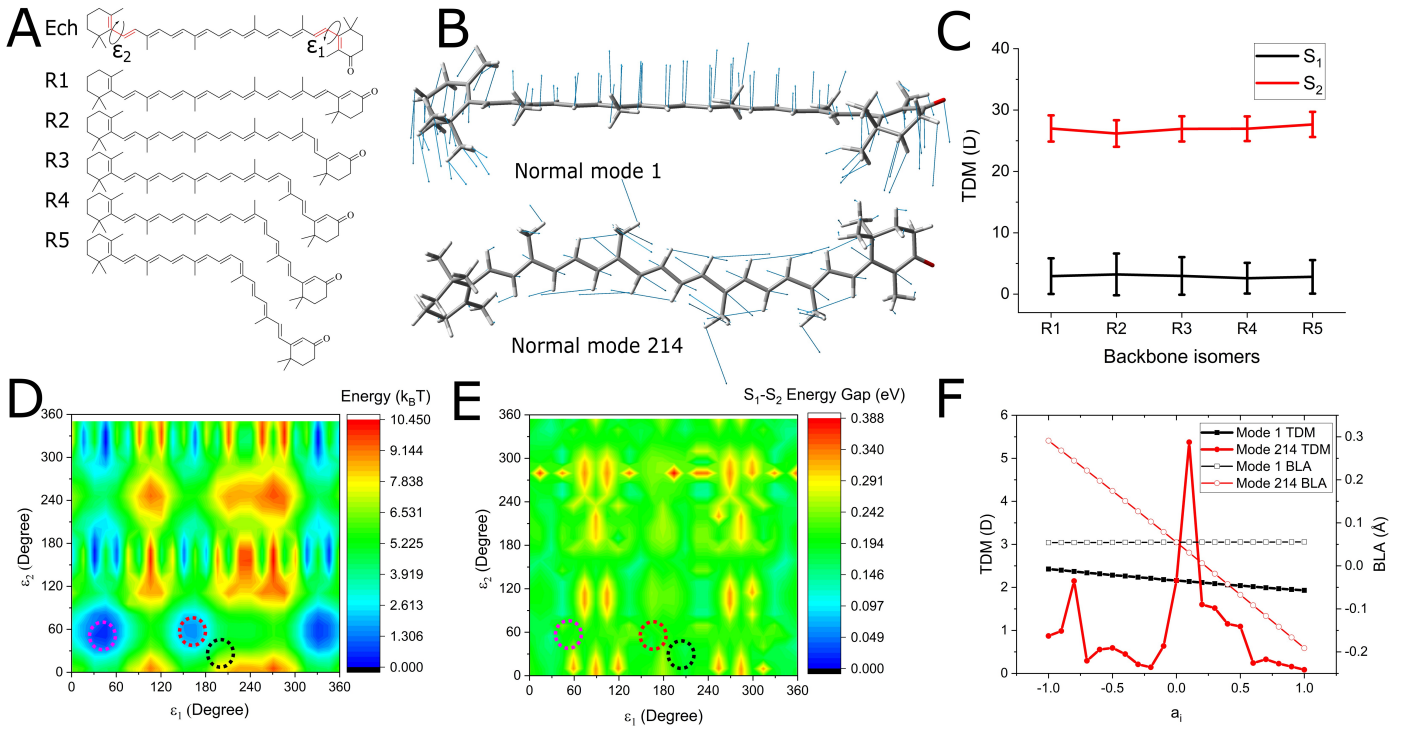

Fig. 1 A. Molecular structures of *cis-cis* Ech (showing the two end-ring dihedrals) and 5 backbone isomers ($R1-R5$). **B**. The atomic displacements associated with the 1^{st} (low frequency) and the 214^{th} (high frequency) normal modes of Ech (in vacuum). The former is responsible for out-of-plane bending, while the high frequency mode is representative of the collection of modes responsible for C=C and C-C stretching. **C**. The average S_1/S_2 TDMs (with standard deviations shown as error bars) of R1 to R5 backbone isomers (in THF) over a short MD run. **D**. Ground state energy surface (in units of k_BT at 300 K) of Ech as a function of the end-ring dihedral angles. The global minimum is at $[\varepsilon_1,\varepsilon_2]$ $[50°, 50°]$ (magenta circle), which represents the *cis-cis* configuration. A local minimum occurs at approximately [165°,60°] (red circle) which corresponds to *cis-trans*. Shown in the black circle is the dihedral angle distribution approximately corresponding to Ech in OCP_o (although the two surfaces are not directly comparable). **E** Variations in the S_1-S_2 energy gap of Ech across the same surface. **F**. Ech BLA and S_1 TDM as a function of normal distortions along the 1^{st} (bending) and 214^{th} (C=C stretch) modes.

TDMs directly output by MOPAC and TDMs calculated from the wave functions given by MOPAC differ by a factor of 2-3, with the later being in reasonable agreement with experiment[46]. The reason for this is unclear but the process of calculating TDMs from first principles for each structural snapshot is prohibitively expensive. We therefore rely on re-scaling the MOPAC TDMs. While these single point values demonstrate our calculation of Ech excited states are at least qualitatively reasonable, the calculation of absorption spectra below provides a more convincing and intuitive validation.

3.2 Non-planar Distortions to Echinenone

We first considered three types of *ad-hoc* deformations: Backbone isomerization, end-ring rotation and normal distortions. Isomerization is the most obvious way in which inversion symmetry is broken and we consider geometries $R1-R5$ as shown in Fig. 1 **A**. In Fig. 1 **C** we plot the average S_1 and S_2 TDM for MD trajectories (in THF) for each with the error bars indicating standard deviations. Although we see relatively large variances for each we see almost no change in the average TDMs. Inversion symmetry has nothing to do with S_1 being optically-forbidden.

End-ring rotations affect the S_1-S_2 energy gap through modulation of effective conjugation length[7] which induce mixing and the *borrowing* of TDM by S_1. Fig. 1 **D** shows the ground state energy (in k_BT at $300K$) for the surface defined by the two end-ring dihedrals $[\varepsilon_1,\varepsilon_2]$ (see Fig. 1 **A**). The global minimum (magenta circle) occurs at around $[50°, 50°]$ which corresponds to a non-planar *cis-cis* configuration and agrees with the 47° calculated previously[65]. At approximately [165°,60°] (red circle) is the local minimum corresponding to cis-trans. We notice that both minima are surrounded by large barriers that significantly hinder movement. Fig. 1 **E**, which shows the variation in S_1-S_2 energy gap across the same surface. Over the entire surface we see that the gap varies from $0.10-0.39$ eV, although the *cis-cis* and *cis-trans* regions both correspond to a gap of $0.20-0.25$ eV. This potentially results in a change in S_1 TDM from ~ 2 D to ~ 4 D between *cis-cis* and *cis-trans* which is due to the change in effective conjugation length. Additional surfaces for S_1 and S_2 transition energies and S_1 TDM are shown in Supp. Fig. 11 of the ESI.

For normal distortions each mode was scanned across $-1 \leq a_i \leq 1$ (see Eq. (2)) and the BLA and S_1 TDM calculated. The full data is difficult to represent but we see two groups of vibrations (one centred around 1100 cm^{-1} and the other 1700 cm^{-1}) that have a strong effect on S_1-S_2 energy gap and therefore S_1 TDM. These are associated with the optically-coupled C-C and C=C stretching modes respectively. In Fig. 1 **F** we show two representative traces. Mode 1 (Fig. 1 **B**) is the low frequency out-of-plane bending and

View Article Online
DOI: 10.1039/C9CP03574E

it has little effect on S_1 TDM and essentially no effect on BLA. This trend is preserved even for distortions as large as $a_1 \sim -20$ (see below). Mode 214 is one of several modes that involve in-plane C=C stretching. It has a calculated frequency of 1551 cm^{-1} which we compare to the Raman-active ν_1 C=C stretching band which occurs at ~ 1550 cm^{-1} [62]. Distortions along this mode have a profound effect on the BLA of the molecule. It also has a strong and seemingly chaotic effect on the S_1 TDM. Two effects were noted firstly, for distortions larger than $|a_{214}| \sim 0.1$ S_1 and S_2 cross, we have corrected for this in Fig. 1 **F** by always denoting the predominantly double $HOMO-LUMO$ state "S_1" regardless of energetic position (although as they approach degeneracy the distinction becomes meaningless). Secondly, as $|a_{214}| > 0.1$ the BLA of the conjugated chain is so strongly-perturbed that the active space becomes unstable and the calculations unreliable (see ESI, Supp. Figs. 3 and 4). Fortunately, actual distortions of this magnitude are energetically inaccessible (it is a very "stiff" mode). Only the steep slope about $a_{214} \sim 0$ is relevant (even in the OCP_o binding pocket the Ech BLA differs little from the equilibrium value) across the calculations are well-behaved. There are several modes (all C=C or C-C stretching modes) that effect S_1 in this manner. Additional plots showing S_1-S_2 energy gap and C_H^L for S_1 as a function of normal distortions are shown in Supp. Figs. 12 and 13 of the ESI.

3.3 Echinenone in THF: Structural Fluctuations

Ech in THF (Fig. 2 **A**) remains in the linear, *cis-trans* configuration throughout all MD trajectories due to the large barriers. In Fig. 2 **B** we show the mean and standard deviation of the normal mode decomposition of Ech snapshots (red). We show only the contribution from Mode 1 and the major BLA-coupled high frequency modes. We have to treat these with caution and remember that they are merely a basis. For the high frequency modes BLA changes associated with similar modes tends to cancel. The mean contribution for each mode is zero but we see large variances for mode 1. This reflects overall bending of the molecule. The deviations associated with the high frequency modes are much smaller but not insignificant. This reflects the fact that some overall twisting of the molecule is accessible. We can combine several high frequency modes to reproduce this twisting without any large net change to BLA. This cancellation effect is seen explicitly when we consider OCP_o. Never-the-less there is some small fluctuation in BLA which induce fluctuations in the S_1 TDM (see Fig. 2 **C**). The average value is $\mu_{S_1} = 1.7D$, slightly smaller than the value calculated at the DFT geometry, and 76% of snapshots have $\mu_{S_1} = 1-2D$. The remainder represent the system sampling twisted structures that induce significant S_1-S_2 mixing. 1% of snapshots represent a maximum of μ_{S_1} $9D$. The clear correlations between BLA, S_1-S_2 energy gap and TDM are shown in Figs. 2 **D**, **E** and **F**. Essentially they show that larger BLA lower the S_1-S_2 energy gap and increases state mixing. This can be intuitively understood as breaking of (the already approximate) p-h symmetry of the back bone and is unrelated to inversion symmetry.

Next we consider the absorption spectrum. Fig. 3 **A** and **B** show the calculated spectral densities (in THF) of S_1 and S_2 respectively, with the numerical data taken directly from MD in black and the ansatz density in red. Both have a structure characteristic of a Car, most notably two strong under-damped peaks at 1100 and 1700 cm^{-1} which correspond to the optically-coupled C-C and C=C vibrations respectively. The width of the peaks come from the fact that multiple normal modes contribute to each. A third, low amplitude peak is present at ~ 500 cm^{-1} implies a small coupling of the states to lower frequency vibrations. The amplitude of the S_1 density is larger than that of S_2 by a factor of ~ 3. This is illustrated in Fig. 3 **C** where we show the high frequency oscillations in S_1 and S_2 excitation energies. This implies that our calculated S_1 state is much more displaced from the ground state than S_2. Translating these into absorption spectra shows that our description of S_2 is surprisingly accurate. Fig. 4 **E** compares our calculated S_2 absorption to that measured by Ushakov *et al.* [66]. Other than a ~ 50 nm shift to align the two spectra (by correcting for the over-estimate of the S_2 energy) no external model was used in constructing this spectrum. The slight discrepancy in width can be attributed to the neglect of both anharmonic effects in our Ech FF (blue edge) and solvatochromic effects in our AM1-MECI calculations. Although the S_1 vibronic structure is less well-characterized experimentally, the amplitude of our spectral density, and therefore the implied S_0-S_1 displacement, are almost certainly over-estimated. Fitting the numerical density to the ansatz directly requires un-physically large reorganization energies, resulting in a lineshape that is extremely broad and vibronically featureless (see Supp. Fig. 14 of the ESI). This is not consistent with two-photon absorption measurements which show a similar width and vibronic profile to S_2 [67]. In Fig. 4 **F** we incorporate the calculated one-photon absorption of S_1 (dotted line), where we have renormalized the amplitude of the spectral density to match that of S_2. Essentially this means we are assuming S_1 has the same vibronic structure as S_2. S_1 appears as a shoulder on the red edge of S_2 with negligible amplitude due to the huge disparity in oscillator strength (Fig. 4 **F** inset).

3.4 Echinenone in OCP_o: Enforced Distortions

In the OCP_o crystal Ech takes on a distorted *cis-trans* structure with the keto end-ring being approximately 48° deviated from a planar *trans* configuration. Previous (and much longer) MD simulations showed that this conformation is meta-stable in solution [65]. In our simulations the end ring of Ech very quickly relaxed to 32° from planar. We attribute this to the fact that we used a specially-parameterized FF rather than a generalized one to better reproduce the stiffness of the conjugated backbone. Following this initial relaxation their is no change in conformation during our MD runs. In Fig. 1 **E** we add a black circle to approximately indicate the region of the potential energy surface on which Ech moves in OCP_o. As with the local minimum it is a region in which the S_1-S_2 energy gap changes a little. This region is associated with an S_1 TDM in the $2-4D$ range compared to $< 2D$ around the global minimum. However, this is for illustrative purposes only and one cannot directly compare the relaxed structure of Ech inside the binding-pocket with an *ad hoc* distortion to the vacuum structure.

View Article Online
DOI: 10.1039/C9CP03574E

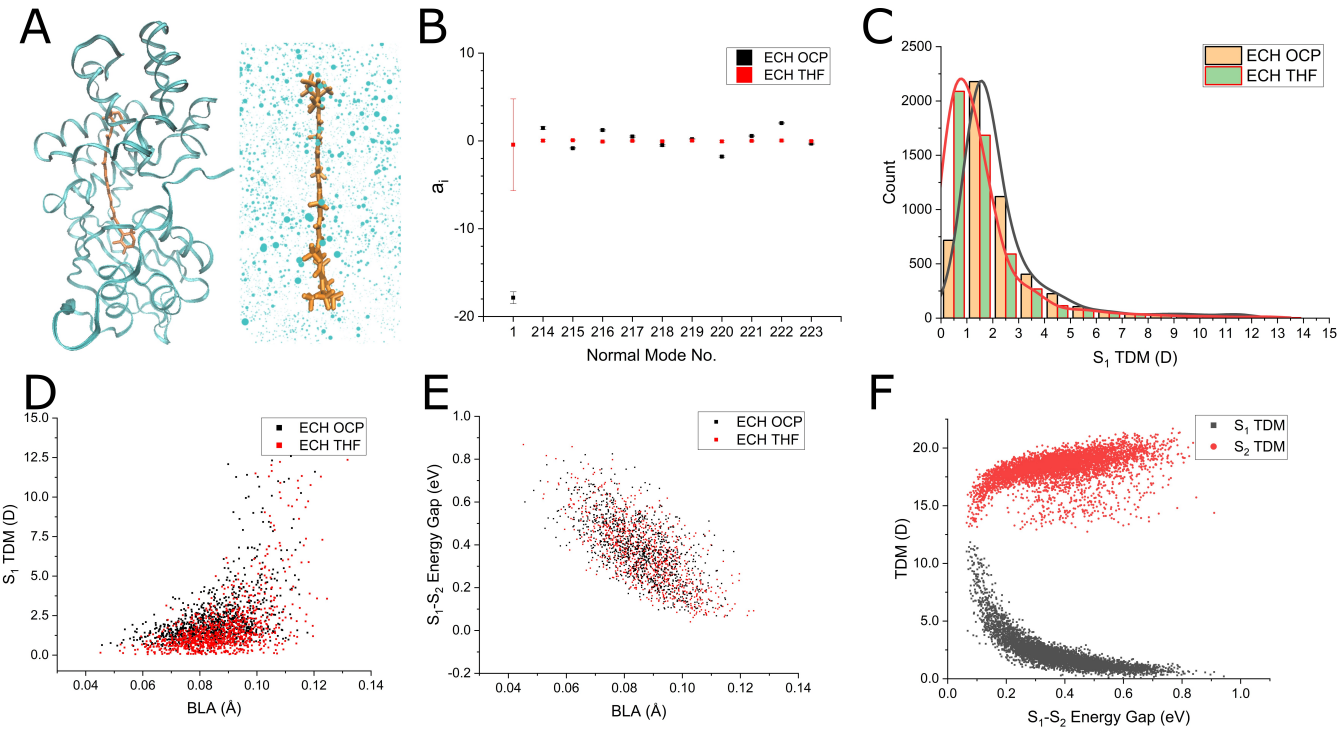

Fig. 2 A. *Left*: Ech embedded in OCP$_o$ (PDB 5TUX) (shown in orange/cyan respectively). *Right*: Ech in an explicit THF environment (solvent shown as dots in cyan). **B**. Partial plot of the variation in normal distortion contributions to Ech in OCP$_o$ (black) and THF (red). **C**. The distributions of S_1 TDM for the Ech snapshots in THF and OCP$_o$. We show these both as a histogram (bin width 1 D) with Ech in THF and OCP$_o$ for the same bin shown side-by-side. **D**. S_1 TMD plotted against backbone BLA for uncorrelated snapshots in THF (red) and OCP$_o$ (black). **E** S_1-S_2 energy gap against BLA for the same structural snapshots. **F**. TDM plotted against S_1-S_2 gap for Ech in THF. Data for Ech in OCP$_o$ is visually identical and so not shown.

The binding pocket also enforces significant distortions to the backbone. Fig. 2 **B** shows that this is predominantly a very large ($a_1 \sim -18$) out-of-plain bending (Mode 1). There are also very large contributions from the high frequency modes ($|a_i| \sim 2$) due to the twisted geometry. Individually these distortions would be inaccessible but the cancellation effect (see modes 214 and 215 for example) prevents any large changes to BLA. The average S_1 TDM (2.3D) is slightly increased relative to Ech in THF (1.7D, Fig. 2 **C**), which we attribute mainly to end-ring orientation and not some net drift in BLA. Fig. 1 **D** and **E** show now difference in the distribution of BLA. In both cases we see large fluctuations in S_1-S_2 energy gap and S_1 TDM caused by small ($\sim$0.06 and $\sim$0.12) fluctuations in BLA (Fig. 2 **E**)

If we compare the calculated S_2 absorption spectra with that of Ech in THF (Fig. 4 **A**) we do not see a significant red-shift (we use the same re-scaling factor) nor do we see any change in width. We do see a slight alteration in vibronic structure with a slightly stronger 0-0 peak. Experimentally, the 0-0 line of OCP$_o$[20] is red-shifted by 20 nm with respect to Ech in THF[66] (Fig. 4 **D**). It is therefore likely that this shift is solvatochromic (we neglect the protein binding pocket in our excited state calculations). Moreover, Fig. 4 **B** shows we do not capture the significant broadening of OCP$_o$. This due to our neglect of solvatochromic effects, hydrogen-bonds, and, more importantly, heterogeneous broadening. OCP$_o$ has been demonstrated to contain at least two spectral sub-populations[62]. Lastly, Fig. 4 **C** features the addition of S_1 absorption. Although there is a net change in oscillator strength (it is larger by a factor of $\sim$ 1.8) relative to Ech in THF, it is still essentially dark.

4 Discussion

The term "symmetry forbidden" has given rise to considerable confusion when discussing S_1 and its role in processes such as NPQ. Generally it is understood in terms of inversion symmetry and even minor deviations from a perfectly linear configuration have been suggested as capable of producing an optically-allowed S_1 state. We have shown that back-bone isomerization has no effect on the S_1 TDM. Actually this can be inferred from the spectral properties of xanthophylls like *9-cis* neoxanthin, but we show it definitively here. Clearly inversion symmetry, or lack there-of, is irrelevant, as argued by Fiedor *et al.*[23] Changes to conjugation, defined by BLA, are the critical factor as was shown previously[34,63]). This can be related back to p-h symmetry but since this is exact only for some *pi*-electron models of idealized linear polyenes it doesn't strictly apply to Cars. "Symmetry forbidden" is therefore inaccurate and confusing.

However, an important question is whether Car conjugation can be significantly perturbed by a protein binding pocket. We show that the OCP$_o$ binding pocket - which is almost unique in the severity of the distortion it enforces on the chromophore - does cause changes in conjugation through alterations in the end-ring orientations. The result is a slight change in the mean S_1 TDM from 1.7 D to 2.3 D. In both THF and OCP$_o$ the calculated S_1 absorption is essentially undetectable and we can say that the

View Article Online
DOI: 10.1039/C9CP03574E

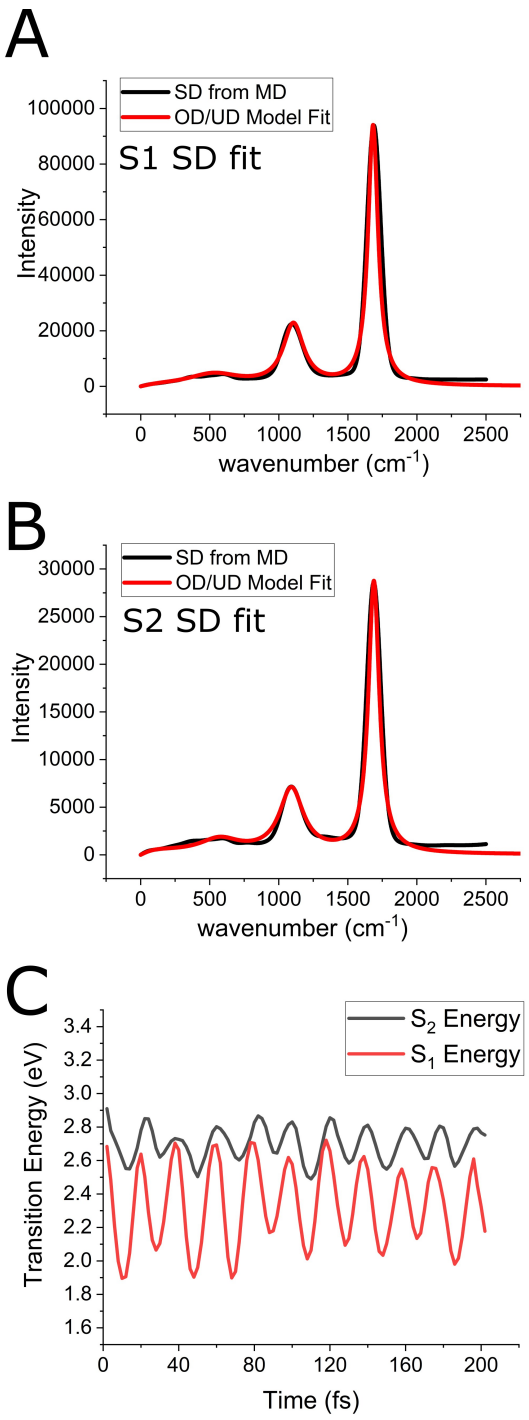

Fig. 3 The calculated vibronic properties of Ech in THF. The equivalent for OCP_o is essentially identical and not shown. **A**. The S_1 spectral density. The purely numerical density (extracted directly from MD) is shown in black. The red line represents a fit to an ansatz spectral density function. **B**. The S_2 spectral density. **C**. Oscillations in the S_1 (red) and S_2 (black) transition energies over 100 frames isolated from a MD trajectory with a time step of 0.5 fs.

unusual red absorption feature in OCP crystals is not related to any "allowed S_1". It is also far too red and must be some effect of long range order that is not obvious from the crystal unit cell. However, we do see some tuning of the S_1 transition density by the binding pocket and it is possible that this could be biologically significant. Similar effects in multi-pigment proteins such as LHCII would alter on the inter-pigment excitonic couplings. However, it is highly unlikely that this is the sole mechanism by which NPQ is switched on and off. The change in S_1 TDM is too small to generate the order of magnitude changes in couplings that are a feature of the NPQ mechanism[14].

Despite little net change in the S_1 TDM we showed that it fluctuates wildly due to optically-coupled high-frequency vibrations altering BLA. These occur on a ~ 20 fs timescale. If the Car potential surface is symmetric (as we have assumed in our calculations) then they will average out to zero. However, if the surface is asymmetric then optical-pumping of the C=C and C-C stretching modes could cause some transient increase in S_1 TDM. It would be interesting to see if this could be detectable in single molecule experiments in which you have ultra-fast coherent excitation of these modes.

In our spectral calculations we found that S_1 has a qualitatively similar vibronic structure to S_2, characterized by optically-coupled C=C and C-C stretching modes. However, the spectral density showed that S_1 was far more displaced from the ground state than S_2. This was argued to be the reason for S_1 being optically-forbidden by Fiedor *et al.*[23] However, this implies unphysically large re-organization energies and a lack of vibronic progression in the spectrum that is at odds with the observed two-photon spectrum. This exaggerated displacement is likely an artifact of the AM1-MECI method. A lack of Frank-Condon overlap with the ground state is likely not the reason for S_1 being forbidden.

In conclusion, We have illustrated how S_1 is optically-forbidden due to the a lack of one-electron transition density which in turn is defined by the degree of conjugation. Even severe distortions cannot cause S_1 to become optically-allowed as alterations to BLA are simply too stiff to be accessible. Small tuning of the transition density is possible but is likely too small to play a critical role in mechanisms such as NPQ. Lastly, the *large-displacement* model of S_1 is not consistent with the spectroscopic properties of Cars.

5 Author Contributions

CD, TW and VB devised the project, with TP and AR providing the initial motivation and key questions. TW carried out the bulk of all theoretical work with support form VB. VB adapted the procedure for computing absorption lineshapes from MD trajectories. TW and CD wrote the paper with input from VB, TP, and AR.

6 Acknowledgements

CD and VB thank the Leverhulme Trust (grant: RPG-2015-337) for financial support, while TW thanks the Chinese Scholarship Council, TP thanks the Czech Science Foundation (18-21631S), and AVR thanks the Royal Society (Wolfson Research Merit Award WM140084). This research utilised Queen Mary's Apocrita HPC facility, supported by QMUL Research-IT.

View Article Online
DOI: 10.1039/C9CP03574E

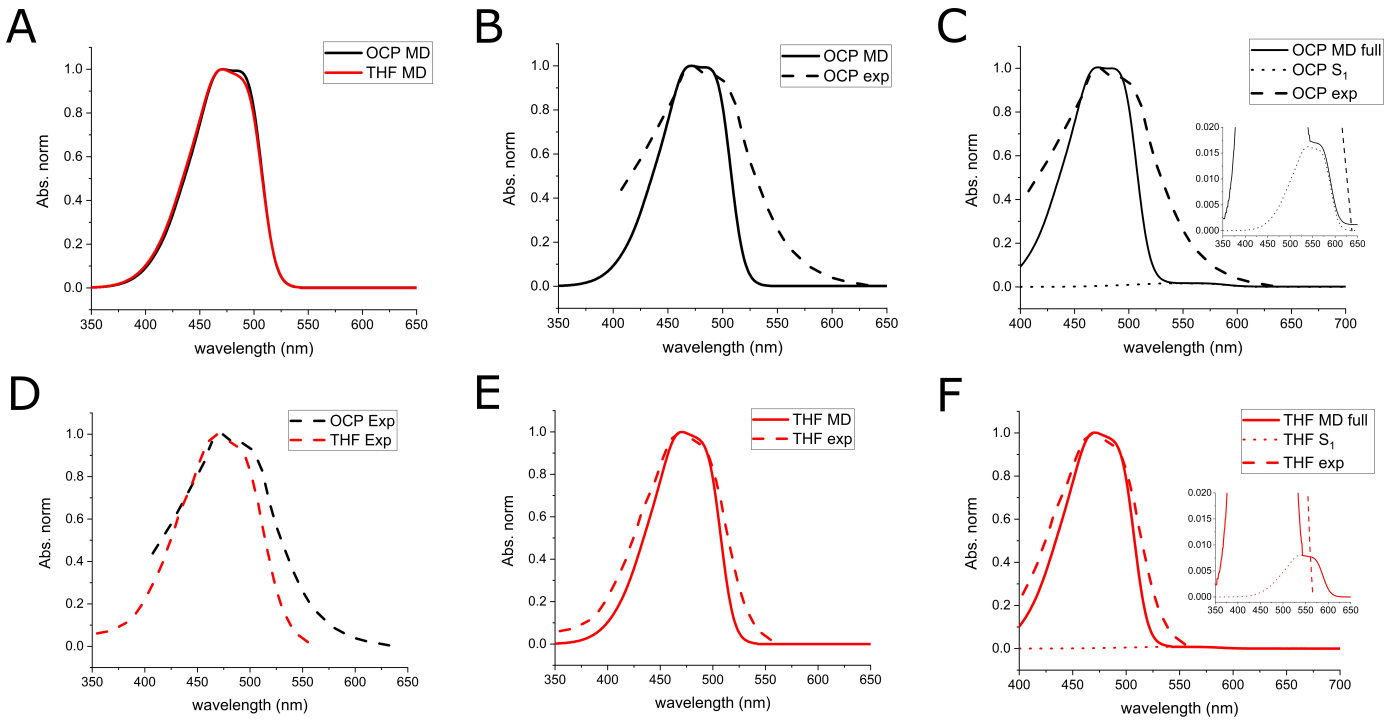

Fig. 4 A. Calculated absorption spectra for Ech in THF (red) and OCP_o (black) generated directly from MD. **B**. Comparison of calculated (solid line) and experimental[20] (dashed line) absorption spectra for OCP_o. **C**. Full calculated spectrum of OCP_o including S_1 (magnified inset). **D**. Experimental absorption spectra for Ech in THF (red)[66] and OCP_o (black)[20]. **E**. Comparison of calculated (solid line) and experimental (dashed line) absorption spectra of Ech in THF. **F**. Full calculated spectrum of Ech in THF including S_1 (magnified inset).

http://doi.org/10.5281/zenodo.438045

References

1 A. Ruban, *The photosynthetic membrane: Molecular mechanisms and biophysics of light harvesting*, John Wiley and Sons, 2013.

2 B. Demmig-Adams, G. Garab, W. W. Adams and Govindjee, *Non-photochemical quenching and energy dissipation in plants, algae and cyanobacteria*, Springer, 2016.

3 A. V. Ruban, *Plant Physiol.*, 2016, **170**, 1903–1916.

4 D. I. G. Bennet, K. Amarnath, S. Park, C. J. Steen, J. M. Morris and G. R. Fleming, *Open Biol.*, 2019, **9**, 190043.

5 R. L. Christensen, M. Goyette, L. Gallagher, J. Duncan, J. DeCoster, J. Lugtenburg, F. J. Jansen and I. van der Hoef, *J. Phys. Chem. A*, 1999, **103**, 2399–2407.

6 Z. F. He, D. Gosztola, Y. Deng, G. Q. Gao, M. R. Wasielewski and L. D. Kispert, *J. Phys. Chem. B*, 2000, **104**, 6668–6673.

7 T. Polívka and V. Sundström, *Chem. Rev.*, 2004, **104**, 2021–2072.

8 M. M. Mendes-Pinto, E. Sansiaume, H. Hashimoto, A. A. Pascal, A. Gall and B. Robert, *J. Phys. Chem. B*, 2013, **117**, 11015–11021.

9 M. Fuciman, G. Keşan, A. M. La Fountain, H. A. Frank and T. Polívka, *J. Phys. Chem. B*, 2015, **119**, 1457–1467.

10 V. Perlik, J. Seibt, L. J. Cranston, R. J. Cogdell, C. N. Lincoln, J. Savolainen, F. Sanda, T. Mancal and J. Hauer, *J. Chem. Phys.*, 2015, **142**, 2124–2134.

11 P. J. Walla, P. A. Linden, K. Ohta and G. R. Fleming, *J. Phys. Chem. A*, 2002, **106**, 1909–1916.

12 A. V. Ruban, R. Berera, C. Ilioaia, I. H. M. van Stokkum, J. T. M. Kennis, A. A. Pascal, H. van Amerongen, B. Robert, P. Horton and R. van Grondelle, *Nature*, 2007, **450**, 575–578.

13 M. Ashfold, S. Bai, S. Bradforth, P. Chabera, J. Cina, C. E. Crespo-Hernaandez, N. das Neves Rodrigues, M. Duchi, G. Fleming, C. Grieco, S. Habershon, M. Haggmark, S. Hammes-Schiffer, S.-T. Hsieh, B. Kohler, H. Lokstein, A. Marcus, T. Martinez, S. Matsika, T. A. A. Oliver, L. Ortiz-RodriÄśguez, T. Polivka, M. Son, V. Stavros, C. Steen, M. Turner, P. J. Walla and J. Woolley, *Faraday Discuss.*, 2019, **216**, 538–563.

14 K. F. Fox, V. Balevicius, J. Chmeliov, L. Valkunas, A. V. Ruban and C. D. P. Duffy, *Phys. Chem. Chem. Phys.*, 2017, **19**, 22957–22968.

15 V. Balevicius Jr., K. F. Fox, W. P. Bricker, S. Jurinovich, I. G. Prandi, B. Mennucci and C. D. P. Duffy, *Sci. Rep.*, 2017, **7**, year.

16 D. Khokhlov and A. Belov, *Biophys. Chem.*, 2019, **246**, 16–24.

17 M. Son, A. Pinnola, S. C. Gordon, R. Bassi and G. S. Schlau-Cohen, *ChemRxiv*, 2019.

18 R. L. Christensen, M. G. I. Galinato, E. F. Chu, R. Fujii, H. Hashimoto and H. A. Frank, *J. Am. Chem. Soc.*, 2007, **129**, 1769–1775.

19 C. Ilioaia, M. P. Johnson, P.-N. Liao, A. A. Pascal, R. van Grondelle, P. J. Walla, A. V. Ruban and B. Robert, *J. Biol. Chem.*, 2011, **286**, 27247–27254.

View Article Online
DOI: 10.1039/C9CP03574E

20 S. Bandara, Z. Ren, L. Lu, X. Zeng, H. Shin, K.-H. Zhao and X. Yang, *Proc. Nat. Acad. Sci. U. S. A.*, 2017, **114**, 6286–6291.
21 N. Liguori, P. Xu, I. H. van Stokkum, B. van Oort, Y. Lu, D. Karcher, R. Bock and R. Croce, *Nat. Commun.*, 2017, **129**, 1994.
22 N. M. Magdaong, A. M. LaFountain, J. A. Greco, A. T. Gardiner, A.-M. Carey, R. J. Cogdell, G. N. Gibson, R. R. Birge and H. A. Frank, *J. Phys. Chem. B*, 2014, **118**, 11172–11189.
23 L. Fiedor, Heriyanto, J. Fiedor and M. Pilch, *J. Phys. Chem. Lett.*, 2016, **7**, 1821–1829.
24 H. Staleva, J. Komenda, M. K. Shukla, V. Slouf, R. Kana, T. Polívka and R. Sobotka, *Nature Chem. Biol.*, 2015, **11**, 287–291.
25 R. Pariser, *J. Chem. Phys.*, 1956, **24**, 250–268.
26 J. Koutecky and J. Paldus, *J. Chem. Phys.*, 2015, **83**, 1722–1735.
27 P. Tavan and K. Schulten, *J. Chem. Phys.*, 1986, **85**, 6602–6609.
28 P. Tavan and K. Schulten, *Phys. Rev. B*, 1987, **36**, 4337–4358.
29 T. Ritz, A. Damjanovic and K. Schulten, *ChemPhysChem*, 2002, **3**, 243–248.
30 H. Hashimoto, C. Uragami, N. Yukihira, A. T. Gardiner and R. J. Cogdell, *J. Roy. Soc. Interface*, 2018, **15**, 20180026.
31 W. Barford, *Electronic and Optical Properties of Conjugated Polymers. Issue 129 of International Series of Monographs on Physics*, Oxford University Press Oxford, 2005.
32 S. R. Marder, C. B. Gorman, B. G. Tiemann, J. W. Perry, G. Bourhill and K. Mansour, *Science*, 1993, **261**, 186–189.
33 D. Loco, F. Buda, J. Lugtenburg and B. Mennucci, *J. Phys. Chem. Lett.*, 2018, **9**, 2404–2410.
34 S. Knecht, C. M. Marian, J. Kongsted and B. Mennucci, *J. Phys. Chem. B*, 2013, **117**, 13808–13815.
35 I. G. Prandi, L. Viani, O. Andreussi and B. Mennucci, *J Comput. Chem.*, 2016, **37**, 981–991.
36 D. Kirilovsky and C. A. Kerfeld, *Nat. Plants (London, U. K.)*, 2016, **2**, 16180.
37 C. A. Kerfeld, M. R. Melnicki, M. Sutter and M. A. Dominguez-Martin, *New Phytol.*, 2017, **215**, 937–951.
38 A. Wilson, J. N. Kinney, P. H. Zwart, C. Punginelli, S. D'Haene, F. Perreau, M. G. Klein, D. Kirilovsky and C. A. Kerfeld, *J. Biol. Chem.*, 2010, **285**, 18364–18375.
39 A. D. Becke, *J. Chem. Phys*, 1993, **98**, 1372–1377.
40 A. D. McLean and G. S. Chandler, *J. Chem. Phys*, 1980, **72**, 5639–5648.
41 R. Krishnan, J. S. Binkley, R. Seeger and J. A. Pople, *J. Chem. Phys*, 1980, **72**, 650–654.
42 M. J. Frisch, G. W. Trucks, H. B. Schlegel, G. E. Scuseria, M. A. Robb, J. R. Cheeseman, G. Scalmani, V. Barone, B. Mennucci, G. A. Petersson, H. Nakatsuji, M. Caricato, X. Li, H. P. Hratchian, A. F. Izmaylov, J. Bloino, G. Zheng, J. L. Sonnenberg, M. Hada, M. Ehara, K. Toyota, R. Fukuda, J. Hasegawa, M. Ishida, T. Nakajima, Y. Honda, O. Kitao, H. Nakai, T. Vreven, J. A. Montgomery, Jr., J. E. Peralta, F. Ogliaro, M. Bearpark, J. J. Heyd, E. Brothers, K. N. Kudin, V. N. Staroverov, R. Kobayashi, J. Normand, K. Raghavachari, A. Rendell, J. C. Burant, S. S. Iyengar, J. Tomasi, M. Cossi, N. Rega, J. M. Millam, M. Klene, J. E. Knox, J. B. Cross, V. Bakken, C. Adamo, J. Jaramillo, R. Gomperts, R. E. Stratmann, O. Yazyev, A. J. Austin, R. Cammi, C. Pomelli, J. W. Ochterski, R. L. Martin, K. Morokuma, V. G. Zakrzewski, G. A. Voth, P. Salvador, J. J. Dannenberg, S. Dapprich, A. D. Daniels, Ã. Farkas, J. B. Foresman, J. V. Ortiz, J. Cioslowski and D. J. Fox, *Gaussian 09 Revision A.1*.
43 J. J. P. Stewart, *MOPAC: a semiempirical molecular orbital program.*, 2016.
44 T. Kusumoto, D. Kosumi, C. Uragami, H. A. Frank, R. R. Birge, R. J. Cogdell and H. Hashimoto, *J. Phys. Chem. A*, 2011, **115**, 2110–2119.
45 M. Macernis, J. Sulskus, C. D. P. Duffy, A. V. Ruban and L. Valkunas, *J. Phys. Chem. A*, 2012, **116**, 9843–9853.
46 J. Chmeliov, W. P. Bricker, C. Lo, E. Jouin, L. Valkunas, A. V. Ruban and C. D. P. Duffy, *Phys. Chem. Chem. Phys.*, 2015, **17**, 15857–15867.
47 K. F. Fox, C. Unlu, V. Balevicius Jr., B. N. Ramdour, C. Kern, X. Pan, M. Li, H. van Amerongen and C. D. P. Duffy, *Biochim. Biophys. Acta, Bioenerg.*, 2018, **1859**, 471 – 481.
48 V. Balevičius, A. G. Pour, J. Savolainen, C. N. Lincoln, V. Lukeš, E. Riedle, L. Valkunas, D. Abramavicius and J. Hauer, *Phys. Chem. Chem. Phys.*, 2015, **17**, 19491–19499.
49 D. Case, D. Cerutti, T. Cheatham, III, T. Darden, R. Duke, T. Giese, H. Gohlke, A. Goetz, D. Greene, N. Homeyer, S. Izadi, A. Kovalenko, T. Lee, S. LeGrand, P. Li, C. Lin, J. Liu, T. Luchko, R. Luo, D. Mermelstein, K. Merz, G. Monard, H. Nguyen, I. Omelyan, A. Onufriev, F. Pan, R. Qi, D. Roe, A. Roitberg, C. Sagui, C. Simmerling, W. Botello-Smith, J. Swails, R. Walker, J. Wang, R. Wolf, X. Wu, L. Xiao, D. York and P. Kollman, *AMBER 2017, University of California, San Francisco*, 2017.
50 P. F. Jan Saam and J. Eargle, *Paratool Plugin, Version 1.5*.
51 C. I. Bayly, P. Cieplak, W. Cornell and P. A. Kollman, *J. Phys. Chem.*, 1993, **97**, 10269–10280.
52 A. Sali and T. L. Blundell, *J. Mol. Biol.*, 1993, **234**, 779 – 815.
53 J. C. Phillips, R. Braun, W. Wang, J. Gumbart, E. Tajkhorshid, E. Villa, C. Chipot, R. D. Skeel, L. Kale and K. Schulten, *J. of Comput. Chem.*, 2005, **26**, 1781–1802.
54 W. Jentzen, X.-Z. Song and J. A. Shelnutt, *J. Phys. Chem. B*, 1997, **101**, 1684–1699.
55 G. Zucchelli, D. Brogioli, A. P. Casazza, F. M. Garlaschi and R. C. Jennings, *Biophys. J.*, 2007, **93**, 2240–2254.
56 V. May and O. Kühn, *Charge and energy transfer dynamics in molecular systems*, Wiley Online Library, 2011, vol. 2.
57 L. Valkunas, D. Abramavicius and T. Mancal, *Molecular excitation dynamics and relaxation: quantum theory and spectroscopy*, John Wiley and Sons, 2013.
58 S. Mukamel, *Principles of nonlinear optical spectroscopy*, Oxford university press New York, 1995, vol. 29.
59 S. Valleau, A. Eisfeld and A. Aspuru-Guzik, *J. Chem. Phys.*, 2012, **137**, 224103.

View Article Online
DOI: 10.1039/C9CP03574E

60 C. Olbrich, J. Strumpfer, K. Schulten and U. Kleinekathofer, *J. Phys. Chem. Lett.*, 2011, **2**, 1771–1776.

61 S. Shim, P. Rebentrost, S. Valleau and A. Aspuru-Guzik, *Biophy. J.*, 2012, **102**, 649 – 660.

62 E. Kish, M. M. M. Pinto, D. Kirilovsky, R. Spezia and B. Robert, *Biochim. Biophys. Acta, Bioenerg.*, 2015, **1847**, 1044 – 1054.

63 R. Spezia, S. Knecht and B. Mennucci, *Phys. Chem. Chem. Phys.*, 2017, **19**, 17156–17166.

64 T. Polívka, P. Chábera and C. A. Kerfeld, *Biochim. Biophys. Acta, Bioenerg.*, 2013, **1827**, 248–254.

65 E. G. Maksimov, E. A. Shirshin, N. N. Sluchanko, D. V. Zlenko, E. Y. Parshina, G. V. Tsoraev, K. E. Klementiev, G. S. Budylin, F.-J. Schmitt, T. Friedrich, V. V. Fadeev, V. Z. Paschenko and A. B. Rubin, *Biophys J.*, 2015, **109**, 595–607.

66 M. Kopczynski, T. Lenzer, K. Oum, J. Seehusen, M. T. Seidel and V. G. Ushakov, *Phys. Chem. Chem. Phys.*, 2005, **7**, 2793–2803.

67 S. Bode, C. C. Quentmeier, P.-N. Liao, N. Hafi, T. Barros, L. Wilk, F. Bittner and P. J. Walla, *Proc. Natl. Acad. Sci. U. S. A.*, 2009, **106**, 12311–12316.